ACS APPLIED ELECTRONIC MATERIALS

pubs.acs.org/acsaelm Article

Electrical and Thermal Dynamics of Self-Oscillations in TaO_x-Based Threshold Switching Devices

Yiqi Yu, Bingyuan Zhao, Jonathan M. Goodwill, Yuanzhi Ma, James A. Bain, and Marek Skowronski*

Cite This: *ACS Appl. Electron. Mater.* 2020, 2, 683−691 Read Online

ACCESS | Metrics & More | Article Recommendations

ABSTRACT: We present experimental results of relaxation oscillations based on the TaO_x threshold switching devices as a function of voltage, load resistance, and the parallel capacitance. Of particular interest are the dynamics of transitions between ON and OFF states of the device which impose an upper limit of the oscillation frequency. The dynamics have been captured by the finite element electrothermal model using only electrical conductivity vs temperature and thermally activated conductivities as input data. The model reproduced current and voltage waveforms and allowed for following the changes in current density and temperature distributions within the device during oscillations. Both undergo significant breathing-mode-type changes in each cycle as the current spontaneously constricts during the capacitance discharge/heating stage. The model points out the possible approaches toward achieving higher oscillation frequencies.

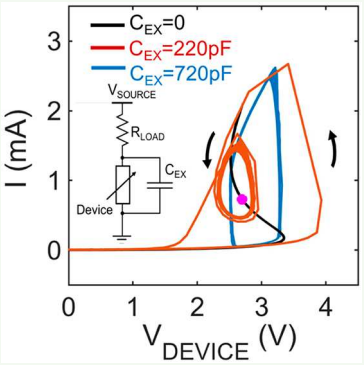

KEYWORDS: *threshold switching, tantalum oxide, negative differential resistance, Poole−Frenkel conduction, oscillation*

1. INTRODUCTION

Many metal/oxide/metal sandwich structures exhibit either S-type negative differential resistance (S-NDR) $I-V$ characteristics[1] or closely related multivalued ones.[2,3] Both lead to threshold switching: an abrupt increase of conductance upon device bias reaching a threshold voltage. In many material systems the NDR $I-V$ characteristics have a thermal origin and are due to electrical conductivity increasing superlinearly with temperature.[4] The devices with S-NDR $I-V$s have been demonstrated by using TaO_x,[2,5,6] NbO_x,[7−11] TiO_x,[5,12] NiO,[13] and VO_2[14−17] as functional layers.

When coupled with a capacitor connected in parallel with the device, the S-NDR results in relaxation oscillations which are of interest for applications in oscillatory neural networks.[18−21] Despite growing interest, a number of issues need to be addressed before such structures will see widespread deployment. Deficiencies of oscillators include inadequate endurance, large energy dissipated per oscillation cycle, and the range of frequencies that is typically limited to below 10 MHz.[22] The current record for the sustained oscillation frequency is 500 MHz and was demonstrated in TiN/TaO_x/TiN vertical structures.[23]

Some insights into the characteristics of oscillations are offered by a simple model of approximating the threshold switch as a device with two states with fixed resistances: an ON state (low resistance) and an OFF state (high resistance).[24−27] The OFF → ON transition takes place when the voltage reaches threshold voltage, V_{TH}, with the reverse transition occurring at the holding voltage, V_{HOLD}. Both transitions are typically assumed to be instantaneous in the simplest model. The oscillation period was calculated as the sum of times required to charge the capacitor through the load and the device in the OFF state and the time of a discharge through load and the device in the ON state. The calculated frequencies agreed with the measured values reasonably well at low frequencies when the rates of internal processes within the device are much faster than the changes in the circuit.[24] What this circuit-oriented model has not addressed is the physics behind threshold switching which dictates the time and the energy required for the device to react to changes of voltage and current. In devices where threshold switching is due to thermal runaway,[2,28,29] the response time is limited by heat capacity of the device and the heat generation rate. This is expected to come into play at frequencies which are of interest for applications in neuromorphic computing. Understanding these switching dynamics is critical for design of devices operating above 1 GHz.[22]

In this report, we present experimental results of the relaxation oscillations in a circuit consisting of TaO_x-based S-NDR device, parallel capacitor, and a load resistor. The current, voltage, and temperature evolution within these devices, with added restrictions imposed by the circuit, are

Received: November 27, 2019
Accepted: February 3, 2020
Published: February 3, 2020

https://dx.doi.org/10.1021/acsaelm.9b00782
ACS Appl. Electron. Mater. 2020, 2, 683−691

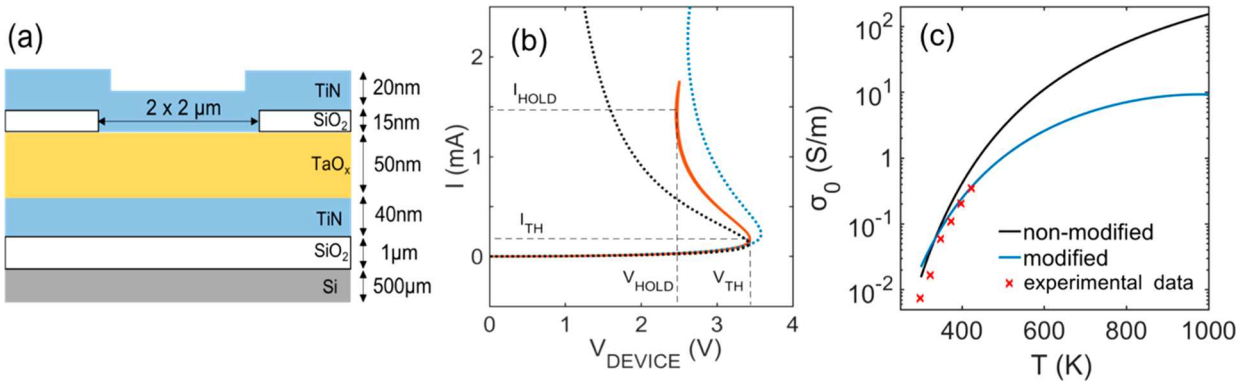

Figure 1. (a) Structure of the device used in this work. (b) Experimental (red solid line, measured with R_{LOAD} = 8 kΩ, and maximum value of V_{SOURCE} was 16.5 V) and simulated quasi-static $I-V$ characteristics obtained with the standard Poole−Frenkel conductivity σ_{PF} (black dotted line) and modified formula σ_{PF}^{M} (blue dotted line). The stage temperature was 300 K in experiment and simulations. (c) Values of low field conductivity as a function of temperature in the Poole−Frenkel model (eq 1) and the modified Poole−Frenkel model σ_{PF}^{M}. The low-temperature activation energy was 0.48 eV, and the donor density $N_D = 10^{18}$ cm^{-3}. Red crosses mark experimental points (see text).

simulated by using a finite element model solving the heat and charge flow equations with the only input data being the dependence of electrical conductivity on electric field and temperature, the values of thermal conductivities of materials, and the device geometry. The agreement between experiment and simulation validates the model.

2. RESULTS AND DISCUSSION

2.1. Quasi-Static *I*−*V* Characteristic. The structure of devices used in this work is shown in Figure 1a. The salient features of the structure include the active area of the device being defined by an insulating SiO_2 layer on top of TaO_x and a functional layer deposited on the flat TiN electrode. This design allowed for elimination of low-density areas associated with shadowing on patterned substrates.[30] Figure 1b displays the quasi-static $I-V$ characteristic (red solid line) measured in a circuit consisting of a voltage source, a load resistor (R_{LOAD}), and the device under test. All experiments reported here as well as simulations have been performed with the stage temperature of 300 K. The value of R_{LOAD} was 43 kΩ, allowing for access to the entire S-NDR characteristic.[1] The voltage sweep rate was 2×10^{-3} V μs^{-1} and was slow enough for the device to reach steady state current and temperature for every value of source voltage. The $I-V$ was symmetric with respect to polarity reversal with only the positive part of the $I-V$ shown in Figure 1b. The quasi-static $I-V$ consists of three segments. The OFF state for current between 0 A and the quasi-static threshold current (I_{TH}), the NDR segment between I_{TH} and holding current (I_{HOLD}), and the low-resistance ON state with positive $\partial I/\partial V$ above I_{HOLD}. The holding voltage and current are defined by the position of the upper "knee" in the S-NDR characteristics. The $I-V$ is similar to that obtained on our crossbar structures[2,31] with one important difference: the patterning of only the top electrode eliminated the problems with the step coverage in deposition of the functional layer and allowed for extending the $I-V$ to higher current values. This revealed the ON branch of $I-V$ characteristics while avoiding permanent changes to the $I-V$.

The experimentally measured device behavior has been simulated by using a finite element model implemented in COMSOL Multiphysics commercial software package and solving the heat and charge flow equations with the added restrictions of the circuit. The detailed description of the equations, boundary conditions, and material parameters can be found in our previous publications.[2,28,31] In distinction to other simulations,[4,10,32−35] we have not assumed uniform temperature and current density in the device solving instead for the position-dependent values of both. This is an important feature of this simulation as the current is expected to constrict within the NDR region, forming a small, high-current-density domain.[1] This phenomenon significantly affects the ON state conductance and dynamics of the ON−OFF transitions. The input data for the simulation included literature values of thermal and electrical conductivities of all materials and the device geometry (Figure 1a). The electrical conductivity of the functional oxide was measured at low field values in the 300−425 K range (Figure 1c) and fitted with the exponential function to determine activation energy and the pre-exponential factor (E_a and P_f in eq 1). We have used this value of E_a in modeling of $I-V$ and oscillations but adjusted P_f to get a better agreement between the quasi-static experimental and simulated values of threshold current. The experimental parameters were used in the Poole−Frenkel (P−F)[36] model of conductivity:

$$\sigma_{PF}(F, T) = \sigma_0\left\{\frac{1}{2} + \frac{1}{F}\left(\frac{kT}{\beta}\right)^2\left[1 + \left(\frac{\beta\sqrt{F}}{kT} - 1\right)\exp\left(\frac{\beta\sqrt{F}}{kT}\right)\right]\right\},$$
$$\beta = \left(\frac{q^3}{\pi\varepsilon_0\varepsilon_i}\right)^{1/2}, \quad \sigma_0 = P_f \exp\left(-\frac{E_a}{kT}\right) \tag{1}$$

where F is the electric field, T is the local temperature, q is the charge of an electron, ε_0 is the permittivity of space, and ε_i is the dielectric constant of TaO_x. This dependence was extrapolated to higher temperatures as needed in the simulation and is shown in Figure 1b as a solid black curve. It should be noted here that the value of P−F conductivity is steeply increasing at 1000 K.

The activation energies of low field electrical conductivity of oxides used as functional layers of threshold switches are typically between 0.215 and 0.6 eV.[10,28,33,37] Because the threshold switching devices can reach temperatures exceeding 1000 K during operation,[34] a significant fraction of traps pinning the Fermi level become ionized. This implies that the Fermi level has to move toward the middle of the gap, reducing the carrier density. In other words, the standard P−F formula overestimates the conductivity at high temperatures and the

https://dx.doi.org/10.1021/acsaelm.9b00782
ACS Appl. Electron. Mater. 2020, 2, 683−691

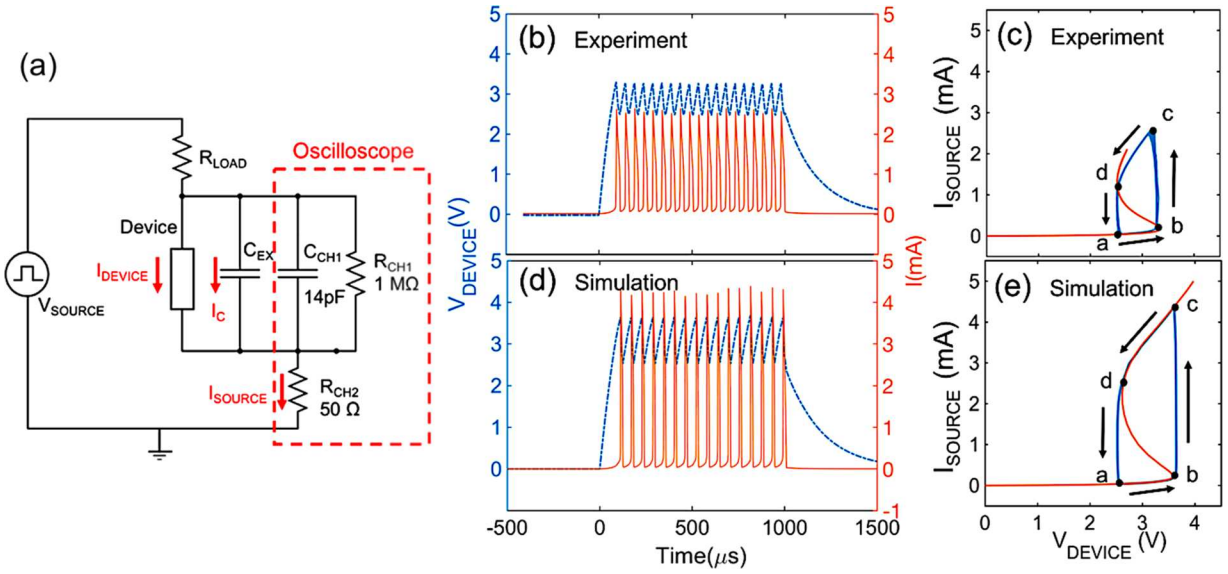

Figure 2. (a) Experimental circuit for oscillation testing. (b) Experimental transients of V_{DEVICE} and I_{SOURCE} in response to the rectangular voltage source pulse 1 ms long with C_{EXT} = 25 nF, R_{LOAD} of 8 kΩ, and V_{SOURCE} = 9 V captured at 300 K. (c) Experimental data in (b) plotted in $I-V$ plane. (d) Simulation of V_{DEVICE} and I_{SOURCE} as a function of time. (e) Data in (d) plotted in $I-V$ plane.

value of current in the ON state. This problem was addressed by solving the neutrality equation for the Fermi energy $E_F(T)$:

$$2\left(\frac{m_e^* kT}{2\pi\hbar^2}\right)^{3/2} \exp\left(\frac{E_F(T) - E_C}{kT}\right) = N_D\left(1 - \frac{1}{1 + \exp\left(\frac{E_D - E_F(T)}{kT}\right)}\right) \quad (2)$$

where the m_e^* is the effective mass of electrons, E_C is the conduction band edge energy, E_D is the donor level energy, and N_D is the density of donors. The estimated $E_F(T)$ was then inserted into the expression for $\sigma_0(T)$:

$$\sigma_0^M(T) = 2q\mu\left(\frac{m_e^* kT}{2\pi\hbar^2}\right)^{3/2} \exp\left(\frac{E_F(T) - E_C}{kT}\right) \quad (3)$$

σ_0^M was then used to replace σ_0 in eq 1, giving the modified Poole–Frenkel conductivity σ_{PF}^M. The pre-exponential factors and activation energies in both equations were extracted from experimental data at low temperatures and fields.

The values of low field conductivity obtained from the formula for σ_{PF}^M are plotted as the solid blue line in Figure 1c. The modified conductivity saturates with increase of temperature much faster than the original P–F dependence with value of conductivity more than an order of magnitude lower than initial model at 1000 K. The $I-V$s calculated with the original and modified conductivities are shown in Figure 1b as dotted black and blue lines, respectively. The modified P–F model shows a better agreement with the experimental $I-V$, but the agreement is far from perfect. The discrepancies likely stem from the imprecise materials data. For example, our measurement setup allowed for the measurements of TaO_x electrical conductivity only up to 425 K and a field of 4×10^6 V m^{-1}, but the formulas 1 and 3 have been extrapolated up to 1000 K and 8×10^7 V m^{-1} and likely deviate from the actual conductivity values. Also, the values of thermal conductivities at high temperatures are not known, and neither are the thermal boundary resistances (assumed to be negligibly small here). This lack of precise input data limits the precision of the simulation results but should allow for prediction of trends.

2.2. Electrical Dynamics of Oscillations. The circuit used for inducing the oscillations and measurements of source current (I_{SOURCE}) and device voltage (V_{DEVICE}) transients is shown in Figure 2a. It consisted of a load resistor (R_{LOAD}) integrated on a chip with the device, an external capacitor connected in parallel with the device (C_{EXT}), a voltage source (V_{SOURCE}), and two channels of an oscilloscope. All oscillation effects in this work were observed at the stage temperature of 300 K. To begin, the current and voltage transients were measured with a large external capacitor (C_{EXT} = 25 nF) and R_{LOAD} = 8 kΩ (Figure 2b). A rectangular V_{SOURCE} pulse with the amplitude of 9 V was applied, starting at t = 0 s and ending at t = 1000 μs. This combination of V_{SOURCE} and R_{LOAD} corresponds to the operating point formed by the intersection of the load line and quasi-static $I-V$ in the middle of the NDR region with the V_{SOURCE} about half of the maximum value used in the sweep experiments. The rising edge of the pulse is only 2 ns, but the V_{DEVICE} increases gradually with time as the parallel capacitor charges until V_{DEVICE} reaches the threshold voltage at t = 92 μs. This is followed by sawtooth-like voltage oscillations with the frequency of 20.4 kHz. After termination of the pulse, the voltage decreases gradually as the capacitor discharges through the device and the load. The transients in Figure 2b have been replotted in the $I-V$ plane as a phase portrait in Figure 2c (solid blue line). This figure also shows the quasi-static $I-V$ data collected separately for reference. One can notice that point "c" on the trajectory loop corresponds to higher current and device voltage than the highest point along the quasi-static $I-V$. The limit of the device voltage/current during dc sweep is due to high temperature reached by the device. Increasing the dissipated power any further led to permanent changes in the device characteristics due to ion motion. During the oscillation experiment the power dissipated at point "c" was higher but was maintained for a very short time, making such an experiment possible.

https://dx.doi.org/10.1021/acsaelm.9b00782
ACS Appl. Electron. Mater. 2020, 2, 683–691

During each oscillation cycle, the device evolves along a trajectory forming a loop consisting of four segments. Part "a" to "b" corresponds to charging the capacitor with the device evolving along the OFF state of the quasi-static $I-V$. Point "b" is located close to the threshold knee of the quasi-static S-NDR curve, at which point the differential resistance reaches zero. At this moment, the capacitor serves as a voltage source with current flowing in the loop consisting of the capacitor and the device. This process corresponds to the almost vertical segment "b" to "c" in Figure 2c. After "c", the loop follows the ON state, as the capacitor discharges. Upon reaching "d" at the holding voltage and current, the device transitions to the OFF state in time corresponding to the device cooling down. In circuits with large capacitance, charging and discharging times are much longer than thermal transitions b → c and d → a with charging time always longer than the discharging time. Similar trajectories of oscillations between quasi-static ON and OFF states with vertical transition segments have been reported in threshold switching devices based on functional materials such as VO_2, NbO_x,[24,38,39] and $Ge_2Sb_2Te_5$.[40]

The oscillations were simulated by using the finite element model similar to the one described above with the difference being the addition of the capacitor in the circuit and applying a rectangular voltage source pulse rather than a voltage sweep. The circuit response was followed as a function of time adjusting the time step as needed. The simulation produced current and temperature distribution within the device at every time step as well as values of voltage and current at every circuit node. The simulation data in Figures 2d and 2e (at 300 K) have reproduced the general shape of the experimental transients and the shape of phase portraits (Figures 2b and 2c). However, there are some significant differences. Among them is the amplitude of the simulated current of 4.2 mA compared to the experimental result of 2.6 mA. This is the direct consequence of the simulated values of current in quasi-static $I-V$ being significantly higher than experimental ones (Figure 1b). This, in turn, is likely due to an overestimate of the TaO_x conductivity at high temperatures. The simulated frequency is lower (17 kHz) than the experimental one (20.4 kHz).

The $I-V$ phase portrait loop in Figure 2c is repeatedly traversed during oscillations. An expanded view of the current and voltage transients corresponding to one oscillation cycle is shown in Figure 3. The four points in time (a through d) corresponding to changes in $\partial I/\partial V$ in Figure 2c are denoted by the vertical red dashed lines. These are close to but not identical to charging and discharging cycles bounded by the extrema of V_{DEVICE} which are marked by black vertical dashed lines with pink and white background colors. When V_{DEVICE} reaches the threshold (point "b"), the current rapidly increases while the V_{DEVICE} keeps increasing for another 2 μs before it reaches a maximum and starts to decrease. The current reaches a maximum after another 2 μs. The delay between corresponding extrema of V_{DEVICE} and I_{SOURCE} is due to the thermal capacitance which slows down the change of temperature and conductivity of the oxide. The V_{DEVICE} is controlled by the parallel capacitor. Because the RC time constant is much larger than the thermal time constant (25 μs vs 0.2 μs), the voltage decreases only a small amount during "b" to "c" with most of the discharge occurring in "c" to "d" segment. After reaching point "d", the device rapidly cools down, transitioning to the OFF state.

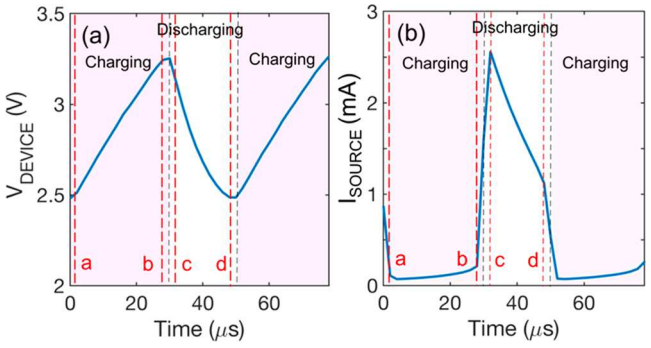

Figure 3. Experimental oscillation waveform in circuit with C_{EXT} = 25 nF, R_{LOAD} of 8 kΩ, and V_{SOURCE} = 9 V: (a) voltage−time trace and (b) current−time trace. Charging and discharging processes of the capacitor are marked by vertical dashed black lines and pink and white background color.

When the R_{LOAD} and V_{SOURCE} are fixed, the oscillation frequency is determined by the capacitance in parallel with the device. When C_{EXT} is reduced to 720 pF, the $R_{EFF}C$ time constant becomes comparable to the thermal time constant of the device. The effective resistance R_{EFF} here is given by a parallel combination of the device resistance and load resistance: $R_{EFF} = (R_{LOAD}R_{DEVICE})/(R_{LOAD} + R_{DEVICE})$. Thus, R_{EFF} is close to R_{LOAD} while the capacitor is charging (= 5.76 μs) and close to R_{DEVICE} in the ON state while the capacitor is discharging (= 1.04 μs).[24] Accordingly, the shape of trajectory in $I-V$ plane changes to that shown as the blue continuous line in Figure 4a. At t = 0, the V_{DEVICE} and current are at the origin of coordinates with the device initially evolving along the OFF state of quasi-static $I-V$. Here, the V_{DEVICE} increases well beyond the threshold voltage during the charging cycle before the trace turns vertical. The trace forms a spiral and, within couple of revolutions, converges to a stable loop centered on the operating point formed by the intersection of the load line (purple dashed line) and the quasi-static $I-V$ (purple dot and dashed line in Figure 4a). The corresponding frequency of the oscillations increased to 370 kHz for this value of capacitance. Points "c" and "d" appear to merge with the loop shape resembling a triangle rather than a quadrilateral due to shorter discharging time (previously segment c → d). Figures 4b and 4c show the voltage and current waveforms obtained with C_{EXT} = 720 pF after the stabilization process. The maximum voltage across the device decreased compared to that obtained with higher parallel capacitance as the stable loop does not reach the quasi-static threshold voltage and the minimum voltage decreases below the quasi-static holding voltage. The peak-to-valley amplitude of current oscillations decreases with the maximum current decreasing and minimum current increasing. One should note that the point of maximum $\partial I/\partial t$ in Figure 4c corresponds to the maximum of V_{DEVICE} and the start of the discharging cycle. At the start of charging cycle when the V_{DEVICE} is increasing, the current keeps dropping due to decreasing temperature.

Lowering the C_{EXT} further to 220 pF with the same operating point increases the frequency to 940 kHz and results in an even smaller stable trajectory loop (Figure 4a). Extrapolating this behavior, one would expect the amplitude of the oscillations to decrease at even lower values of capacitance with the loop eventually collapsing to the operating point. The salient features of the behavior observed in the experiments described above are discussed together with results of simulations (section 2.4) and after the description of

https://dx.doi.org/10.1021/acsaelm.9b00782
ACS Appl. Electron. Mater. 2020, 2, 683−691

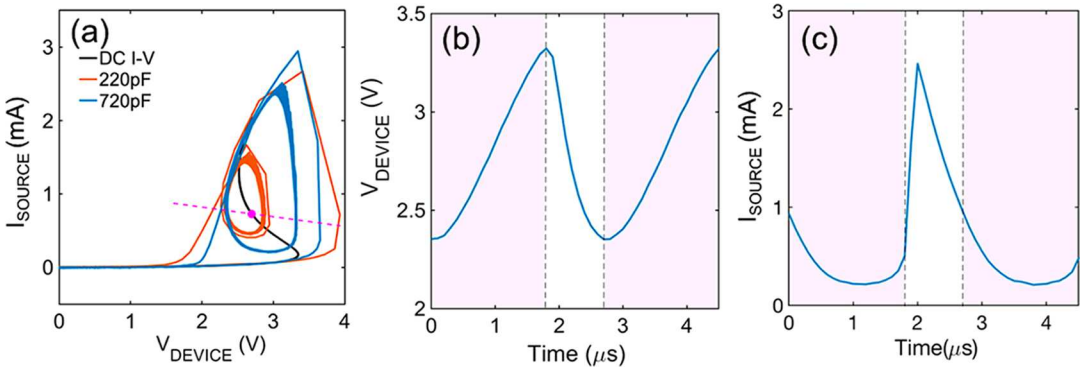

Figure 4. (a) Experimental phase portraits of oscillations corresponding to two different values of capacitance (220 and 720 pF) biased to the same operating point marked by the pink point on quasi-static $I-V$ (V_{SOURCE} = 9 V, R_{LOAD} = 8 kΩ). The black curve represents the experimental quasi-static $I-V$. (b) V_{DEVICE} waveform and (c) I_{SOURCE} waveform for capacitance of 720 pF. Charging and discharging cycles are marked by pink and white background colors.

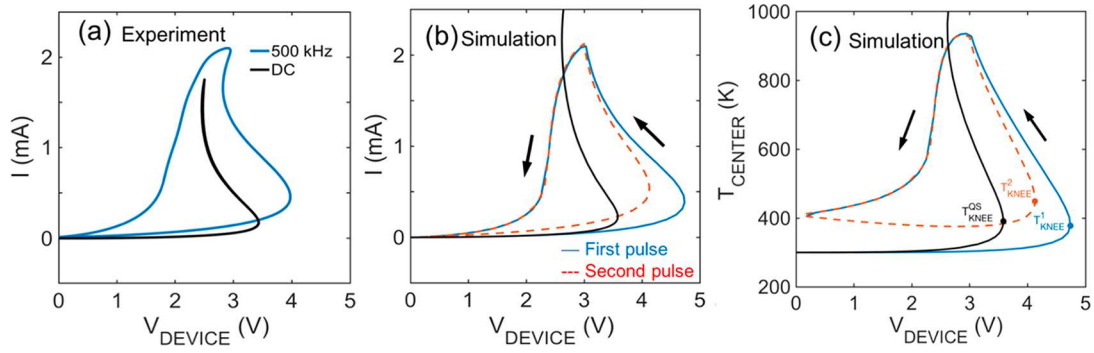

Figure 5. (a) Experimental $I-V$ characteristic corresponding to voltage source sweep rate of 500 kHz (blue loop) and the quasi-static $I-V$ with a load resistance of 8 kΩ in series (all at 300 K). (b) Simulated $I-V$ during the first two voltage sweeps with the same sweep rate. (c) Evolution of the temperature at the center of the device during the first two sweeps shown in (b). Continuous blue curve for the first sweep and dashed red curve for the second one. Black line corresponds to the temperature during quasi-static sweep.

changes in $I-V$ and device temperature with the increasing voltage sweep rate (section immediately following).

2.3. Transient Characteristics Measurements and Modeling. The importance of the thermal dynamics of the oxide-based threshold switches is demonstrated by $I-V$ characteristics measured with high voltage sweep rates (Figure 5a). To avoid the $I-V$ being affected by the discharge of parasitic capacitances, we have used a circuit with no external capacitor and only one channel of the oscilloscope monitoring the I_{SOURCE}. The V_{DEVICE} was calculated by using the values of V_{SOURCE}, measured I_{SOURCE}, and known load resistance. The bias consisted of a continuous series of triangular pulses with a constant amplitude of 20 V and the frequency of 500 kHz. R_{LOAD} was 8 kΩ, and the stage was at room temperature. The $I(t)$ and $V(t)$ exhibited an initial stabilization period of changing amplitudes corresponding to device temperature increasing from 300 K to the average temperature under ac bias. Only the steady state sweep is shown in Figure 5a as a continuous blue loop with the black trace representing quasi-static $I-V$. The fast sweep $I-V$ exhibits a large hysteresis between up and down sweeps with the threshold knee appearing at voltage much above quasi-static V_{TH} during the sweep up and the NDR region disappearing in the sweep down.

The circuit response to initial pulses was captured by simulation. Figure 5b shows the simulated current as a function of voltage during first two pulses. The blue solid line displays the $I-V$ trajectory during the first pulse with the red dashed line depicting the trajectory during the second sweep. The knee voltage decreases between the first and second pulse and stabilizes with subsequent ones with the knee voltage remaining larger than the quasi-static V_{TH}. The corresponding simulated temperature evolution is shown in Figure 5c with the blue continuous line corresponding to the first sweep and dashed red line the second one. Black curve represents simulated temperature during quasi-static sweep. The temperature during the first sweep up stays below the quasi static one as the device does not have enough time to reach steady state temperature at intermediate values of voltage. The temperature corresponding to the knee during the first sweep (marked with a blue dot and symbol T^1_{KNEE}) is 390 K and is close to the value of knee temperature during the quasi-static sweep (378 K and black dot denoting T^{QS}_{KNEE}) as was argued by Li et al.[41] and Gibson.[4] This explains the increased V_{DEVICE} at the knee: during faster sweep, the V_{DEVICE} will reach a higher value in the time it takes to reach the same critical temperature. During the sweep down, the temperature and current stay higher than during the quasi-static sweep with the temperature at 0 V being about 100 K above the stage temperature. An important point to note here is that the decrease of current during the sweep down occurs at voltages below the holding voltage of the simulated quasi-static $I-V$.

During the second and subsequent sweeps, initially the temperature continues to slowly decrease, reaching the minimum of 376 K at about 2.8 V. The "knee" temperature T^2_{KNEE} increases to 460 K, and during the sweep down the

https://dx.doi.org/10.1021/acsaelm.9b00782
ACS Appl. Electron. Mater. 2020, 2, 683−691

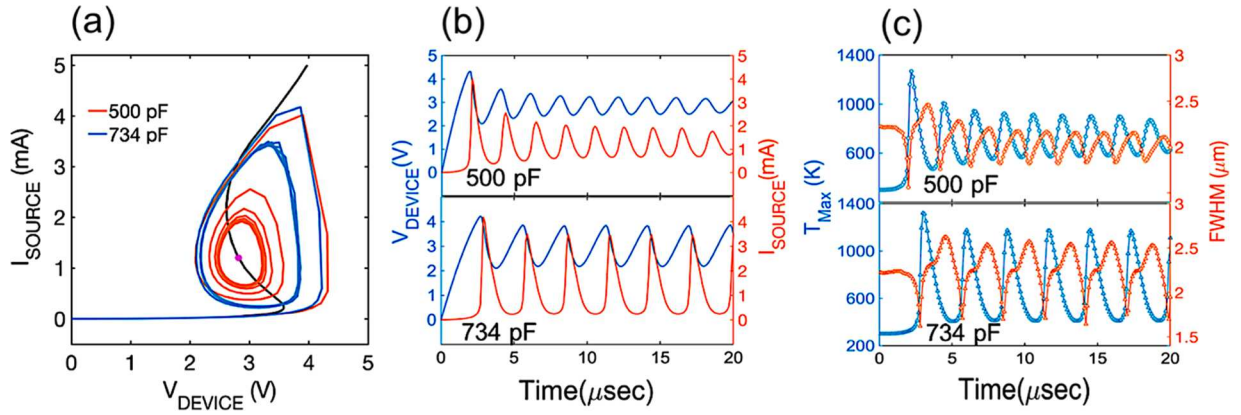

Figure 6. (a) Simulated phase portrait at the same operating point and capacitance of 500 and 734 pF. (b) Transients of I_{SOURCE} and V_{DEVICE} for the first several oscillation cycles. (c) Corresponding temperature at the center of device and the full width at half-maximum (FWHM) of temperature distribution as a function of time during the oscillations.

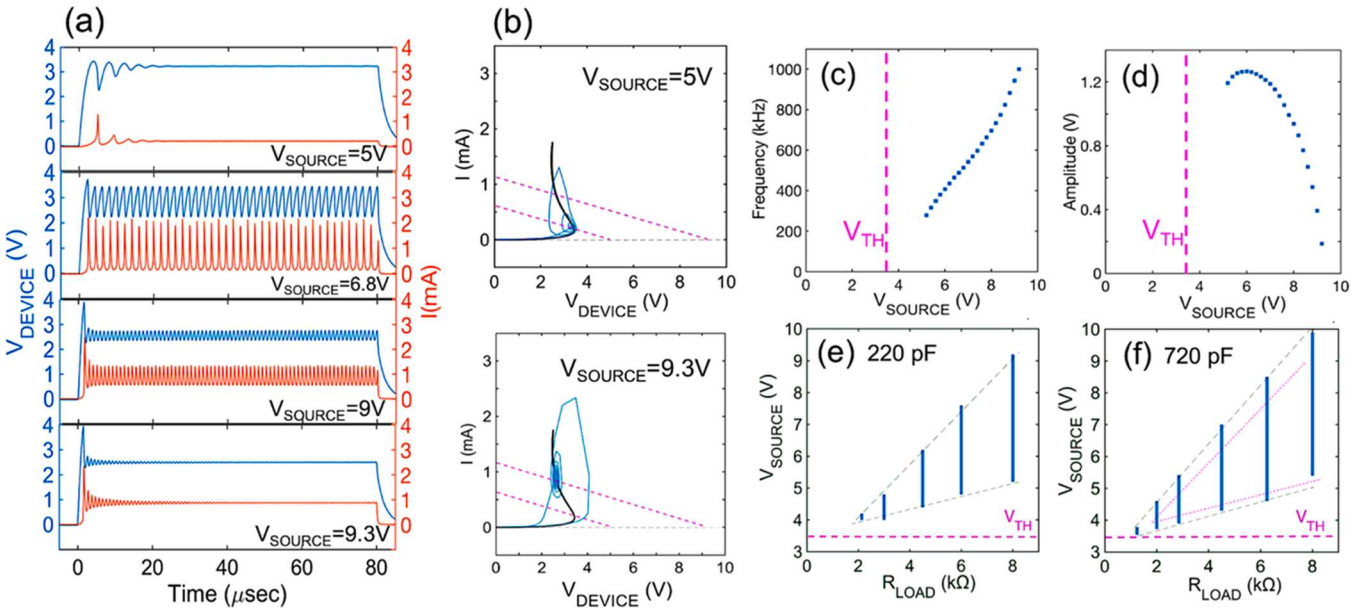

Figure 7. (a) Experimental device voltage and source current transients for different values of V_{SOURCE} (C_{EXT} = 220 pF, R_{LOAD} = 8 kΩ). (b) Phase portraits of damped oscillations at values of V_{SOURCE} close to lower and upper "knee" of the $I-V$. Corresponding load lines are included in both figures to make the comparison easier. (c) Dependence of oscillation frequency on V_{SOURCE} and (d) oscillation amplitude (peak to peak) as a function of V_{SOURCE}. (e) Tested range of V_{SOURCE} values resulting in stable oscillations as a function of load resistance for C_{EXT} = 220 pF. The range is marked as vertical blue bars at different values of R_{LOAD}. Dashed black lines serve as a guide to the eye. (f) Same as (e) for C_{EXT} = 720 pF marked by blue bars and black dashed lines. The range for 220 pF is marked for comparison with (e) by purple lines.

temperature almost perfectly repeats the first sweep. The second loop is in fact the steady-state loop. The minimum temperature effectively becomes the stage temperature for the fast sweep $I-V$. The expected consequences include lower threshold voltage, higher threshold current, and higher holding voltage.[28] Changes similar to the ones observed during the fast sweep experiment could be expected during high-frequency oscillations.

2.4. Oscillation Modeling. Figure 6a shows the simulated $I-V$ trajectories of the device biased to the operating point on simulated $I-V$ similar to the one in Figure 4a and parallel capacitances of 734 pF (equals C_{EXT} in Figure 4a plus C_{INPUT} of the oscilloscope) and 500 pF. We have used higher capacitance than in the experiment to maintain the oscillations that decayed to zero with lower C_{EXT} in simulation. The frequency with which trajectory is traversed increases with a decrease of C_{EXT}, and the area of the trajectory diminishes. The data are replotted in Figure 6b as $I(t)$ and $V(t)$ for the first several cycles while Figure 6c shows the evolution of temperature at the center of the device and the FWHM of temperature distribution for both values of C_{EXT}.

The transients obtained with 500 pF capacitance exhibit a pronounced "turn on" effect. The trajectory evolves along a spiral which after the third turn converges to a stable loop. This corresponds to the amplitude of the temperature oscillations (as well as the maximum temperature) decreasing with the cycle number as the device did not cool to the stage temperature of 300 K. The value of current at the bottom of the loop is determined by the minimum device temperature. This temperature is increasing with the frequency similarly as the temperature of the OFF state increased for fast voltage sweeps (Figure 5c). The maximum temperature and current

https://dx.doi.org/10.1021/acsaelm.9b00782
ACS Appl. Electron. Mater. 2020, 2, 683−691

are lower than ones for C_{EXT} = 734 pF due to capacitance holding less charge and storing less energy. This energy apparently is not high enough to increase the device temperature to the point on the ON segment of $I-V$ characteristics. This point of view binds the amplitude of oscillations with the value of capacitance and the device size.

The range of V_{DEVICE} values changes with the increase of frequency. The maximum V_{DEVICE} decreases as a function of frequency (Figure 6a) as the effective device temperature increases and the corresponding threshold voltage decreases. In parallel, the minimum voltage is increasing due to the increasing holding voltage. The overall trends in the simulated $I-V$ loop replicate the trends observed in the experiment.

A characteristic feature of threshold switches is the nonuniformity of current and temperature distributions.[1] When the device is biased into the NDR region, the current density is expected to bifurcate into high- and low-current-density domains.[1,2] Because current density is directly tied to the local temperature through eqs 1 and 3, we discuss only the one, namely, the temperature. Figure 6c shows the time evolution of highest temperature in the device (T_{MAX}, located at the center of the device[2,17,28]) and its FWHM. Both the T_{MAX} and FWHM exhibit stable oscillations after the initial 10 μs. The FWHM changes between 1.7 and 2.6 μm—a change of over 50% with the heated volume expanding and shrinking in a typical "breathing" mode fashion. The change is clearly significant and could be even more pronounced in devices with steeper dependence of conductivity on temperature. The smallest FWHM occurs at the time of fastest temperature change. This is a similar behavior to the one reported by Goodwill et al. during a singular threshold switching events.[31] Similar breathing mode behavior of the current constriction has been reported in VO_2-based devices.[42,43]

2.5. Source Voltage Range for Sustained Oscillations.

It is generally accepted that the relaxation oscillations in a circuit consisting of an S-NDR device, a capacitor, a load resistor, and a voltage source occur only when the load line intersects the quasi-static $I-V$ within the NDR region.[27,44] Our experimental and simulation results agree with this conclusion with both the continuous and damped oscillations occurring only when the operating point was in the NDR region. However, this is not the sole requirement for the appearance of sustained oscillations. Figure 7a shows the experimental values of V_{DEVICE} and I_{SOURCE} as a function of time during the rectangular voltage pulse with C_{EXT} = 220 pF and R_{LOAD} 8 = kΩ for four different values of V_{SOURCE}. For V_{SOURCE} of 6.8 and 9 V, the circuit responded with oscillations of constant frequency and amplitude after an initial temperature stabilization period. For V_{SOURCE} values of 5 or 9.3 V, the response was that of damped oscillations with amplitude decreasing to zero within about 10 μs. The corresponding experimental phase portrait spirals with V_{SOURCE} values of 5 or 9.3 V (Figure 7b) collapse to the corresponding operating points. The purple lines in Figure 7b are load lines for R_{LOAD} displaying the boundaries between sustainable oscillations and damped oscillations. The intersections of the purple lines and zero current are the V_{SOURCE} at boundaries. Inspection of the figure reveals that the intersections are located a little above the threshold knee and a little below the holding point, but both were within the NDR. The likely reason is the presence of unaccounted for losses in the circuit. The argument developed by Lavizzari et al.[27] based on the circuit containing load resistor and parallel capacitor indicated circuit instability if the ratio $(R_{LOAD} + R')/R_{LOAD}R'$ is negative. Here, R' is the differential device resistance at the operating point, and accordingly, the oscillation window should extend from threshold to holding voltage. If there is an additional resistance in series with device (R_S) and parallel to the capacitor, the ratio $(R_{LOAD} + R' + R_S)/R_{LOAD}(R' + R_S)$ will be positive for $R' + R_S > 0$. This narrows the operating window on both sides as observed in the experiment. Similar behavior, i.e., damped oscillations occurring within NDR and close to the V_{TH} and V_{HOLD}, has been reproduced in the simulations. It could be due to part of the functional layer close to electrodes which act as the heat sink. This part of the oxide is not heating up as effectively as the middle of the layer and serves as an additional load resistor.

The frequency and the amplitude of oscillations can be tuned by changing the V_{SOURCE} as shown in Figures 7c and 7d (data were obtained in the experiments). Because the V_{SOURCE} must be larger than the V_{TH}, we have marked the V_{TH} value (3.4 V) as the vertical purple dashed lines. The frequency increases monotonically with V_{SOURCE} from 277 kHz to 1 MHz for C_{EXT} = 220 pF and R_{LOAD} = 8 kΩ. A similar increase of frequency with V_{SOURCE} has been reported in number of papers.[23,26,39] The amplitude shows a maximum inside the window and decreases toward zero at both upper and lower boundaries of sustained oscillations.

The boundaries of the window for V_{SOURCE} are shown as a function of load resistor as the black dashed lines in Figure 7e for 220 pF and in Figure 7f for 720 pF (data were obtained in experiments). The window gradually narrows with decreasing R_{LOAD} and closes at a voltage near V_{TH} and the R_{LOAD} value corresponding to the maximum negative differential resistance of the device. The minimum R_{LOAD} depends weakly on the capacitance and decreases with increase of C_{EXT} as is clear from comparison of Figures 7e and 7f. One should also note that the window of V_{SOURCE} broadens for any value of R_{LOAD} with increase of capacitance.

The last point to be made concerns the formation of high current density/high temperature domains predicted to form in threshold switches when biased into the NDR region.[1] In the above discussion, we have used the electrothermal model developed by Li et al.[17,37] and Goodwill et al.[2,28,31] to describe such domains. The model predicts gradually changing temperature and current density within domains, their position in the center of the device, and increasing current constriction with increasing source voltage. The model was confirmed experimentally by numerous experiments in two materials systems: TaO_x[2,28,31] and VO_2.[17,37] Recently, another model of unstable states in NDR devices has been proposed by Kumar and Williams, who suggested that domains should form randomly and should have a uniform temperature and current density.[45] Such domains should have distinctly different dynamics than the ones considered here. In the analysis above, we have been able to account for all experimental observations using analysis of Goodwill et al. and provided a strong argument that this analysis not only applies to the steady state distributions of current and temperature but also accounts for the transient states as well.

3. CONCLUSIONS

We have explored the effect of thermal dynamics in TaO_x threshold switching devices during self-induced relaxation oscillations. The device voltage and source current waveforms were monitored as a function of source voltage, capacitance in

https://dx.doi.org/10.1021/acsaelm.9b00782
ACS Appl. Electron. Mater. 2020, 2, 683−691

parallel with the device, and the load resistor. The experimental trends were replicated by an electrothermal finite element model based on the thermal runaway process which quantitatively described the external parameters of the oscillations (voltage and current waveforms) as well as the transient states of the device (current and temperature distributions). Their salient feature is the current constriction within the device exhibiting breathing mode oscillations. The model can be used to design the devices oscillating at frequencies above 1 GHz.

4. EXPERIMENTAL SECTION

Devices used in this work were inverted via structures with a planar TiN bottom electrode, a TaO_x functional layer, and a 2×2 μm^2 opening in the insulating SiO_2 on top defining the contact area with the top electrode. The entire structure was deposited on 1 μm thick thermal insulator SiO_2 on Si. The 50 nm thick TaO_x layer was reactively sputtered at room temperature with 2.3 sccm O_2 and 57.7 sccm Ar flow into the chamber at pressure of 3 mTorr. TiN electrodes are RF sputtered with 60 sccm Ar flow at 150 W power. The bottom electrode was formed by patterning a blanket TiN layer. All other layers were formed by using a lift-off process. An on-chip serpentine resistor was patterned near the device region bottom electrode.

AUTHOR INFORMATION

Corresponding Author

Marek Skowronski − *Department of Materials Science and Engineering, Carnegie Mellon University, Pittsburgh, Pennsylvania 15213, United States;* orcid.org/0000-0002-2087-0068; Email: ms3s@andrew.cmu.edu

Authors

Yiqi Yu − *Department of Materials Science and Engineering, Carnegie Mellon University, Pittsburgh, Pennsylvania 15213, United States;* orcid.org/0000-0003-2970-6800

Bingyuan Zhao − *Department of Materials Science and Engineering, Carnegie Mellon University, Pittsburgh, Pennsylvania 15213, United States*

Jonathan M. Goodwill − *Department of Materials Science and Engineering, Carnegie Mellon University, Pittsburgh, Pennsylvania 15213, United States;* orcid.org/0000-0002-3466-3350

Yuanzhi Ma − *Department of Materials Science and Engineering, Carnegie Mellon University, Pittsburgh, Pennsylvania 15213, United States;* orcid.org/0000-0002-9901-7659

James A. Bain − *Department of Electrical and Computer Engineering, Carnegie Mellon University, Pittsburgh, Pennsylvania 15213, United States*

Complete contact information is available at: https://pubs.acs.org/10.1021/acsaelm.9b00782

Notes

The authors declare no competing financial interest.

ACKNOWLEDGMENTS

We thank the Carnegie Mellon University Nanofab staff for their support in device development. This work was supported in part by NSF Grant DMR-1905648 and the Data Storage Systems Center at Carnegie Mellon University.

REFERENCES

(1) Ridley, B. K. Specific Negative Resistance in Solids. *Proc. Phys. Soc., London* **1963**, *82* (6), 954−966.

(2) Goodwill, J. M.; Ramer, G.; Li, D.; Hoskins, B. D.; Pavlidis, G.; McClelland, J. J.; Centrone, A.; Bain, J. A.; Skowronski, M. Spontaneous Current Constriction in Threshold Switching Devices. *Nat. Commun.* **2019**, *10* (1), 1628.

(3) Nandi, S. K.; Nath, S. K.; El Helou, A.; Li, S.; Liu, X.; Raad, P. E.; Elliman, R. G. Current Localisation and Redistribution as the Basis of Discontinuous Current Controlled Negative Differential Resistance in NbOx. *Adv. Funct. Mater.* **2019**, *29*, 1906731.

(4) Gibson, G. A. Designing Negative Differential Resistance Devices Based on Self-Heating. *Adv. Funct. Mater.* **2018**, *28*, 1704175.

(5) Sharma, A. A.; Noman, M.; Abdelmoula, M.; Skowronski, M.; Bain, J. A. Electronic Instabilities Leading to Electroformation of Binary Metal Oxide-Based Resistive Switches. *Adv. Funct. Mater.* **2014**, *24* (35), 5522.

(6) Goodwill, J. M.; Sharma, A. A.; Li, D.; Bain, J. A.; Skowronski, M. Electro-Thermal Model of Threshold Switching in TaOx-Based Devices. *ACS Appl. Mater. Interfaces* **2017**, *9* (13), 11704−11710.

(7) Chopra, K. L. Current-Controlled Negative Resistance in Thin Niobium Oxide Films. *Proc. IEEE* **1963**, *51*, 941.

(8) Vezzoli, G. C. Recovery Curve for Threshold-Switching NbO2. *J. Appl. Phys.* **1979**, *50* (10), 6390−6397.

(9) Liu, X.; Sadaf, S. M.; Son, M.; Park, J.; Shin, J.; Lee, W.; Seo, K.; Lee, D.; Hwang, H. Co-Occurrence of Threshold Switching and Memory Switching in Pt/NbO2/Pt Cells for Crosspoint Memory Applications. *IEEE Electron Device Lett.* **2012**, *33* (2), 236−238.

(10) Slesazeck, S.; Mahne, H.; Wylezich, H.; Wachowiak, A.; Radhakrishnan, J.; Ascoli, A.; Tetzlaff, R.; Mikolajick, T. Physical Model of Threshold Switching in NbO2 Based Memristors. *RSC Adv.* **2015**, *5*, 102318−102322.

(11) Funck, C.; Menzel, S.; Aslam, N.; Zhang, H.; Hardtdegen, A.; Waser, R.; Hoffmann-Eifert, S. Multidimensional Simulation of Threshold Switching in NbO 2Based on an Electric Field Triggered Thermal Runaway Model. *Adv. Electron. Mater.* **2016**, *2* (7), 1600169.

(12) Chopra, K. L. Avalanche-Induced Negative Resistance in Thin Oxide Films. *J. Appl. Phys.* **1965**, *36* (1), 184.

(13) Ielmini, D.; Cagli, C.; Nardi, F. Resistance Transition in Metal Oxides Induced by Electronic Threshold Switching. *Appl. Phys. Lett.* **2009**, *94* (6), 063511.

(14) Cope, R. G.; Penn, A. W. High-Speed Solid-State Thermal Switches Based on Vanadium Dioxide. *J. Phys. D: Appl. Phys.* **1968**, *1* (2), 161.

(15) Duchene, J. C.; Terraillon, M. M.; Pailly, M.; Adam, G. B. Initiation of Switching in VO2 Coplanar Devices. *IEEE Trans. Electron Devices* **1971**, *18*, 1151.

(16) Son, M.; Lee, J.; Park, J.; Shin, J.; Choi, G.; Jung, S.; Lee, W.; Kim, S.; Park, S.; Hwang, H. Excellent Selector Characteristics of Nanoscale VO2 for High-Density Bipolar ReRAM Applications. *IEEE Electron Device Lett.* **2011**, *32* (11), 1579−1581.

(17) Li, D.; Sharma, A. A.; Gala, D. K.; Shukla, N.; Paik, H.; Datta, S.; Schlom, D. G.; Bain, J. A.; Skowronski, M. Joule Heating-Induced Metal-Insulator Transition in Epitaxial VO2/TiO_2 Devices. *ACS Appl. Mater. Interfaces* **2016**, *8* (20), 12908.

(18) Taketa, Y.; Kato, F.; Nitta, M.; Haradome, M. New Oscillation Phenomena in VO2 Crystals. *Appl. Phys. Lett.* **1975**, *27* (4), 212−214.

(19) Lalevic, B.; Shoga, M. Relaxation Oscillators in NbO2 Thin Film Switching Devices. *Thin Solid Films* **1981**, *75*, 199.

(20) Schmidt, P. E.; Callarotti, R. C. Theoretical and Experimental Study of the Operation of Ovonic Switches in the Relaxation Oscillation Mode. I. The Charging Characteristic during the off State. *J. Appl. Phys.* **1984**, *55* (8), 3144−3147.

(21) Schmidt, P. E.; Callarotti, R. C. The Operation of Thin Film Chalcogenide Glass Threshold Switches in the Relaxation Oscillation Mode. *Thin Solid Films* **1977**, *42*, 277−282.

(22) Zhao, B.; Ravichandran, J. Low-Power Microwave Relaxation Oscillators Based on Phase-Change Oxides for Neuromorphic Computing. *Phys. Rev. Appl.* **2019**, *11* (1), 1.

(23) Sharma, A. A.; Li, Y.; Skowronski, M.; Bain, J. A.; Weldon, J. A.; et al. *IEEE Trans. Electron Devices* **2015**, *62* (11), 3857−3862.

(24) Kishida, H.; Ito, T.; Nakamura, A.; Takaishi, S.; Yamashita, M. Current Oscillation Originating from Negative Differential Resistance in One-Dimensional Halogen-Bridged Nickel Compounds. *J. Appl. Phys.* **2009**, *106* (1), 016106.
(25) Murdoch, B. J.; McCulloch, D. G.; Partridge, J. G. Synaptic Plasticity and Oscillation at Zinc Tin Oxide/Silver Oxide Interfaces. *J. Appl. Phys.* **2017**, *121* (5), 054104.
(26) Kim, H. T.; Kim, B. J.; Choi, S.; Chae, B. G.; Lee, Y. W.; Driscoll, T.; Qazilbash, M. M.; Basov, D. N. Electrical Oscillations Induced by the Metal-Insulator Transition in VO2. *J. Appl. Phys.* **2010**, *107* (2), 023702.
(27) Lavizzari, S.; Ielmini, D.; Lacaita, A. L. A New Transient Model for Recovery and Relaxation Oscillations in Phase-Change Memories. *IEEE Trans. Electron Devices* **2010**, *57* (8), 1838−1845.
(28) Goodwill, J. M.; Sharma, A. A.; Li, D.; Bain, J. A.; Skowronski, M. Electro-Thermal Model of Threshold Switching in TaOx-Based Devices. *ACS Appl. Mater. Interfaces* **2017**, *9* (13), 11704−11710.
(29) Slesazeck, S.; Mähne, H.; Wylezich, H.; Wachowiak, A.; Radhakrishnan, J.; Ascoli, A.; Tetzlaff, R.; Mikolajick, T. Physical Model of Threshold Switching in NbO2based Memristors. *RSC Adv.* **2015**, *5* (124), 102318−102322.
(30) Xu, Q.; Ma, Y.; Skowronski, M. Nanoscale Density Variations in Sputtered Amorphous TaOx Functional Layers in Resisrive Switching Devices. *J. Appl. Phys.* **2020**, *127*, 055107.
(31) Goodwill, J. M.; Gala, D. K.; Bain, J. A.; Skowronski, M. Switching Dynamics of TaOx-Based Threshold Switching Devices. *J. Appl. Phys.* **2018**, *123* (11), 115105.
(32) Gibson, G. A.; Musunuru, S.; Zhang, J.; Vandenberghe, K.; Lee, J.; Hsieh, C.-C.; Jackson, W.; Jeon, Y.; Henze, D.; Li, Z.; Williams, R. S. An Accurate Locally Active Memristor Model for S-Type Negative Differential Resistance in NbOx. *Appl. Phys. Lett.* **2016**, *108* (2), No. 023505.
(33) Wang, Z.; Kumar, S.; Wong, H. S. P.; Nishi, Y. Effect of Thermal Insulation on the Electrical Characteristics of NbOxthreshold Switches. *Appl. Phys. Lett.* **2018**, *112* (7), 073102.
(34) Kumar, S.; Wang, Z.; Davila, N.; Kumari, N.; Norris, K. J.; Huang, X.; Strachan, J. P.; Vine, D.; Kilcoyne, A. L. D.; Nishi, Y.; Williams, R. S. Physical Origins of Current and Temperature Controlled Negative Differential Resistances in NbO2. *Nat. Commun.* **2017**, *8* (1), 4−9.
(35) Hennen, T.; Bedau, D.; Rupp, J.; Funck, C.; Menzel, S.; Grobis, M.; Waser, R.; Wouters, D. Hennen.Pdf. In IEEE 11th International Memory Workshop (IMW); Monterey, CA, 2019.
(36) Frenkel, J. On Pre-Breakdown Phenomena in Insulators and Electronic Semi-Conductors [3]. *Phys. Rev.* **1938**, *54* (8), 647−648.
(37) Li, D.; Goodwill, J. M.; Bain, J. A.; Skowronski, M. Scaling Behavior of Oxide-Based Electrothermal Threshold Switching Devices. *Nanoscale* **2017**, *9*, 14139−14148.
(38) Liu, X.; Li, S.; Nandi, S. K.; Venkatachalam, D. K.; Elliman, R. G. Threshold Switching and Electrical Self-Oscillation in Niobium Oxide Films. *J. Appl. Phys.* **2016**, *120* (12), 124102.
(39) Chen, P.-Y.; Seo, J.; Cao, Y.; Yu, S. Compact Oscillation Neuron Exploiting Metal-Insulator-Transition for Neuromorphic Computing. *2016 IEEE/ACM Int. Conf. Comput. Des.* **2016**, 1−6.
(40) Ielmini, D.; Mantegazza, D.; Lacaita, A. L. Voltage-Controlled Relaxation Oscillations in Phase-Change Memory Devices. *IEEE Electron Device Lett.* **2008**, *29* (6), 568−570.
(41) Li, D.; Sharma, A. A.; Shukla, N.; Paik, H.; Goodwill, J. M.; Datta, S.; Schlom, D. G.; Bain, J. A.; Skowronski, M. ON-State Evolution in Lateral and Vertical VO2threshold Switching Devices. *Nanotechnology* **2017**, *28*, 405201.
(42) Bortnikov, S. G.; Aliev, V. S.; Badmaeva, I. A.; Mzhelskiy, I. V. VO2 Film Temperature Dynamics at Low- Frequency Current Self-Oscillations. *J. Appl. Phys.* **2018**, *123* (7), No. 075701.
(43) Aliev, V. S.; Bortnikov, S. G.; Mzhelskiy, I. V.; Badmaeva, I. A. Current Oscillations as a Manifestation of Spatio-Temporal Inhomogeneity of Temperature Distribution in Vanadium Dioxide Films at Semiconductor-Metal Phase Transition. *Appl. Phys. Lett.* **2014**, *105* (14), 142101.
(44) Callarotti, R. C.; Schmidt, P. E. Theoretical and Experimental Study of the Operation of Ovonic Switches in the Relaxation Oscillation Mode. II. the Discharging Characteristics and the Equivalent Circuits. *J. Appl. Phys.* **1984**, *55* (8), 3148−3152.
(45) Kumar, S.; Williams, R. S. Separation of Current Density and Electric Field Domains Caused by Nonlinear Electronic Instabilities. *Nat. Commun.* **2018**, *9* (1), 23505−23509.

https://dx.doi.org/10.1021/acsaelm.9b00782
ACS Appl. Electron. Mater. 2020, 2, 683−691